Geomechanics and Engineering, *Vol. 28, No. 3 (2022) 209-224*
https://doi.org/10.12989/gae.2022.28.3.209

Near-explosion protection method of π-section reinforced concrete beam

Qixin Sun[a] and Chao Liu*

Department of Bridge Engineering, Tongji University, Shanghai, 200092, P.R. China

(Received June 15, 2021, Revised December 6, 2021, Accepted December 28, 2021)

Abstract. In this study, the numerical analysis model of π-beam explosion is established to compare and analyze the failure modes of the π-beam under the action of explosive loads, thus verifying the accuracy of the numerical model. Then, based on the numerical analysis of different protection forms of π beams under explosive loads, the peak pressure of π beam under different protection conditions, the law of structural energy consumption, the damage pattern of the π beam after protection, and the protection efficiency of different protective layers was studied. The testing results indicate that the pressure peak of π beam is relatively small under the combined protection of steel plate and aluminum foam, and the peak value of pressure decays quickly along the beam longitudinal. Besides, as the longitudinal distance increases, the pressure peak attenuates most heavily on the roof's explosion-facing surface. Meanwhile, the combined protective layer has a strong energy consumption capacity, the energy consumed accounts for 90% of the three parts of the π beam (concrete, steel, and protective layer). The damaged area of π beam is relatively small under the combined protection of steel plate and aluminum foam. We also calculate the protection efficiency of π beams under different protection conditions using the maximum spalling area of concrete. The results show that the protective efficiency of the combined protective layer is 45%, demonstrating a relatively good protective ability.

Keywords: π-section concrete beam; explosion protection; failure mode; near-field explosion; pressure peak; protection efficiency

1. Introduction

Bridge, a significant role in the transportation network and national infrastructure, plays an important part in the national economy's status. The reinforced concrete bridges is one of the common types of bridges, which has the characteristics of simple structure, low cost, and long durability. The widely used beam structure is reinforced concrete π-section beams, mainly for highway bridges and railway bridges (Kee *et al.* 2019, Shadabfar *et al.* 2020). In recent years, due to the frequent terrorist activities, people have paid more attention to the safety of important infrastructure, including bridge structures. Meanwhile, due to the increase in traffic volume, accidental explosions of vehicles on the bridge also frequently occur. Considering the above reasons, many scholars have carried out a series of studies on the anti-blast performance and durability of bridges.

Through the concrete beam explosion test research found that as the distance from the burst center decreases, the cracking length of the beam increases, and thus the beam is prone to bending failure. At the same time, it is found that as the proportion of stirrups increases and the spacing decreases, the degree of beam explosion damage gradually reduces and with the increase of explosive equivalent, the damage of prestressed steel bars intensified (Zhang *et al.* 2013, Yao *et al.* 2016, Han *et al.* 2019).

Castedo *et al.* (2015) verified and analyzed the numerical simulation of reinforced concrete slabs under explosive loads based on field explosion test data. Aoude *et al.* (2015) studied the anti-blast performance of ultra-high-performance concrete (UHPC) columns. They found that the utilization of UHPFRC significantly improves the explosive performance of reinforced concrete columns and reduces the maximum displacement and residual displacement. Chen *et al.* (2020, 2021) established numerical rust expansion model for the moment of concrete surface rupture and relationship model between the expansion force of corrosion of steel bars and the surface strain of concrete. Xu *et al.* (2021) studied the composite materials and proposed an analytical method to examine the internal crack development in glass fiber reinforced polymer–sea sand concrete composites.

However, it is difficult to conduct on-site full scale structural explosion tests since the blasting test is always costly, time-consuming, labor-intensive, and even dangerous. High-fidelity numerical models are adopted to reliably predict the response of structures under explosive loads to address these issues. Through numerical simulation of concrete structure explosion, it is found that the maximum mid-span deflection of concrete beams with initial cracks increased under the action of explosive loads. Meanwhile, a two-step numerical method which can be used to predict the damage state, stress, displacement response is proposed, and a simplified blast load prediction method to study the cross-sectional response mechanism of side concrete spalling in slender reinforced concrete members under explosive loading based on numerical simulation is proposed (Qu *et al.* 2016, Li and Hao 2011,

---

*Corresponding author, Associate Professor
E-mail: lctj@tongji.edu.cn
[a]Ph.D. Student

http://www.techno-press.org/?journal=gae&subpage=7

ISSN: 2005-307X (Print), 2092-6219 (Online)

Williams and Williamson 2012). Wang (2014) conducted a simulation analysis of a bridge, of which structure failed due to accidental fireworks explosion. This study used engineering calculations and numerical simulations to construct mathematical models of the explosion equivalent and the response of the bridge structure caused by the explosion. Nagy *et al.* (2021) present a complete model simulating the whole buried reinforced concrete structures system which included simulation of the explosion, propagation of shock waves through the soil medium, the interaction of the soil with the buried structure and the structure response needs to be simulated in a single model. Abedini and Zhang (2021) derived analytical formulas to assess vulnerability of RC columns under the explosive loads using an advanced numerical modelling approach. The generated empirical formulae can be used by the designers to predict a damage degree of new column design when consider explosive loads.

Given the strong destructiveness of the explosion load and the corresponding quick structure failure, many scholars have researched the new structure form and the protection method for structures under explosive loads and explosion-proof materials. Through the study of anti-explosion performance of different protective materials, a new type of explosion protection system is proposed, which employs an additive honeycomb core sandwich panel to reduce the impact load caused by a near explosion and contact detonation. And the study found that the metal foam layer as a porous solid can absorb high explosion energy, it can protect the reinforced concrete slab from explosive loads (Qi *et al.* 2017, Wu and Sheikh 2013). Mou and Bai (2018) presented an experimental investigation on the seismic behavior of a novel steel-concrete composite beam-to-column connections reinforced by outer-annular-stiffener. Li *et al.* (2018a) conducted an explosion study on high-strength reinforced concrete beams, and the study showed that the impact of high-strength concrete on the explosive performance of reinforced concrete beams is limited. Feng *et al.* (2017) studied the explosive performance of FRP reinforcement plates through explosion tests, the results of which showed that the concrete slab strengthened by FRP bars has a strong ability to recover from deformation. The mixed-mode debonding of the FRP–concrete interface will be analyzed by a cohesive zone model (CZM) derived from the modified Mohr–Coulomb strength criterion (Zhang *et al.* 2021).

In summary, previous studies mostly focused on the anti-blast performance of concrete members under explosive loads. However, there is little attention to the anti-explosion protection of the π beam structure, especially on the utilization of utilizing different protective materials and different protection forms in the explosion protection of the π beam. To tackle the aforementioned critical issues, we propose establishing a π-beam structure anti-blast finite element model and verifying the accuracy of the numerical model through existing anti-blast tests. We have separately studied the effects of CFRP fiber layer, steel plate layer, ultra-high-performance concrete (UHPC) layer, and combined protective layer of the thin steel plate and foamed aluminum on the explosion protection performance and protection efficiency of π beams. In addition, we also studied the changing law of the pressure peak of the π beam structure under different protection forms and the law of the pressure peak distribution along the longitudinal direction of the beam. Second, we analyze the energy consumption laws of π beams under different protection conditions and summarize the protection capabilities of π beam protection layers from the perspective of structural energy consumption. Finally, combining the parameters of the damaged area of the π beam with studying the protection efficiency of different protection conditions, we implement analysis for both π beam explosion damage mode under different protection conditions and damaged area parameters, in order to determine the optimal protection form of the π beam structure under different explosion loads.

2. *π*-beam near-explosive load action mechanism and analysis condition settings

2.1 Mechanism of the near-explosive load

When an explosive explodes, a fierce chemical reaction occurs, releasing a large amount of energy in the form of heat and light within a short period (RKM FEMA 426 2003). The surrounding air expands rapidly, forming a shock wave of high temperature and pressure, and the energy spreads outward in the form of shock waves, causing huge damage to the surrounding materials. In the process of shock wave propagation, if the explosion shock wave encounters a denser object, the shock wave will rapidly generate a reflected wave with a pressure value greater than the incident pressure value on the contact surface. Under the combined action of the reflected wave and the incident wave, the overpressure peak and impulse acting on the structure are strengthened (Kinney and Graham 1985). The magnitude and duration of the reflected pressure depend on the peak value of the incident wave, the angle of incidence, the distance between the explosive and the reflecting surface, and the reflecting surface (Hetherington and Smith 1994). The relationship between the pressure of the reflected wave and the incident wave at a certain point in the free field during the explosion propagation process is shown in (ASCE Task Committee 1997, TM 5-855-1 1986).

When the explosion shock wave acts on the beam, there are two types of damage to the beam structure caused by the explosion load, namely local damage and overall damage (Zhang *et al.* 2019). After the explosion, if the beam has an explosive through hole, the concrete beam partially forms a blast hole and the concrete peels off, then it is local damage. Suppose under explosive load, the main beam undergoes overall flexural deformation and shear deformation, the structure may undergo overall failure, including overall shear failure, overall bending failure or bending-shear failure with ductile deformation and flexural cracks (Shi *et al.* 2008). When the beam structure is exposed to a near-field explosion, the shape of the explosion shock wave distributed on the surface of the structure is more concentrated than that of the evenly distributed explosion wave in the far-field. Explosive impact loads may lead to

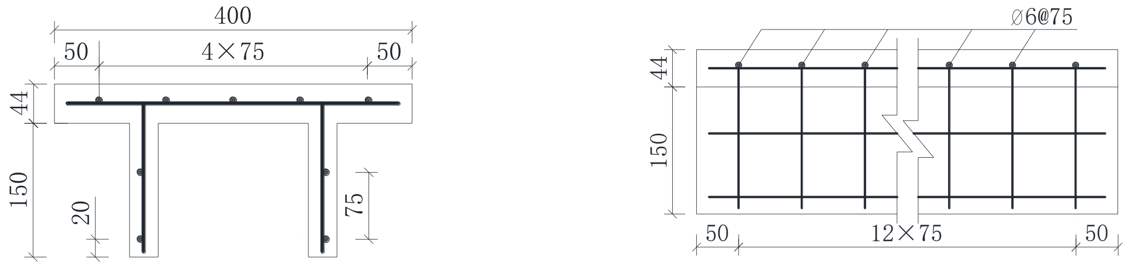

(a) Cross section size and reinforcement (b) Longitudinal section size and reinforcement

Fig. 1 π beam specimen size and reinforcement (mm)

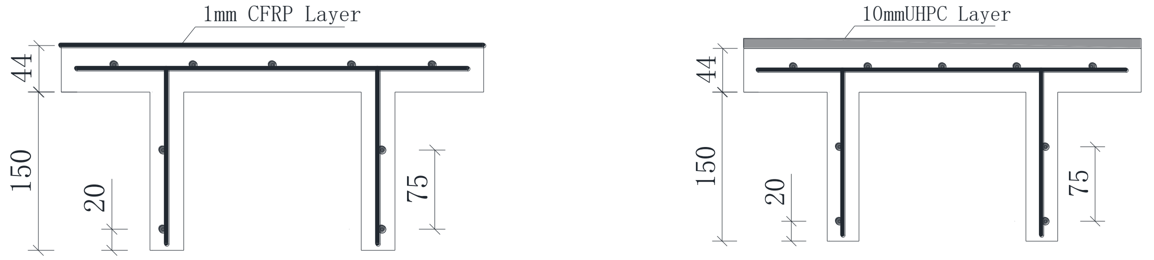

(a) CFRP protective layer (b) UHPC protective layer

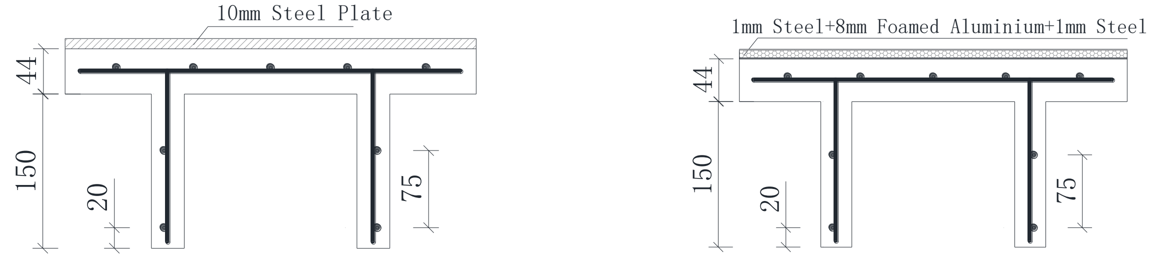

(c) Steel plate protective layer (d) Combined protective layer

Fig. 2 π beam protection conditions setting diagram (mm)

local damage to concrete beams (Yan *et al.* 2015). The degree of spalling damage of beams under explosive loads depends largely on the shear resistance and bonding resistance, as well as the restraint effect of steel bars on the beam concrete.

2.2 Explosion analysis conditions of π-beam specimens

Li *et al.* (2018b) conducted an explosion test study on 15 reinforced concrete π beams under explosive load and obtained relatively complete test data. The paper selects the B series π-beam specimens to consider different forms of explosion protection in the literature (Li *et al.* 2018b). The TNT explosive is 100 g, and the detonation distance from the mid top surface of the π beam is 7.5 cm. The total length of the π beam specimen is 1000 mm, and 194 mm for total height, 44 mm for the top plate thickness. The steel bars in the beams are all ribbed steel bars (HRB235) with a diameter of 6 mm. The standard yield strength is 235 MPa, and the concrete compressive strength of the π beam is 38 MPa. The detailed dimensions and the layout of the steel bars of the π beam specimen are shown in Fig. 1.

The paper will conduct a series of comparison experiments, including not taking protective measures, using CFRP fiber protection, steel plate protection, ultra-high-performance concrete protection (UHPC) and combined protection layer (steel plate + foam aluminum + steel plate) to conduct explosion protection research. The specific settings of the explosion conditions are shown in Fig. 2.

3. Establishment and verification of finite element model

3.1 Material model

The numerical analysis model of π beam was established by using LS-DYNA software. The model uses Shell 163 elements to simulate the CFRP layer, and uses Solid164 eight-node elements and single-point integration to simulate the π-shaped beam, steel plate protection layer, UHPC protection layer, and combined protection layer. The Shell 163 element is only used to display dynamic analysis and is a 4-node unit with curved and membrane characteristics. The element has 12 degrees of freedom at each node. The Solid 164 element is used for dynamic explicit analysis only, and the nodes have degrees of freedom for translation, velocity, and acceleration in X, Y, and Z directions. The steel bar is simulated by Beam161 element, which is only used for explicit dynamic analysis

Table 1 Parameters table of TNT explosive materials

ρ/kg.m^{-3}	$D\ (m/s)$	$PC\ (J/Pa)$	$Beta$	k	G	$SIGY$
1600	6930	21.15×10^9	0.0	0.0	0.0	0.0

Table 2 Equation parameter table of TNT explosive material

A/Pa	B/Pa	R_1	R_2	w	$E_0\ (J/m^3)$	V_0
3.74×10^{11}	3.75×10^9	4.15	0.9	0.35	7×10^9	1.0

Table 3 Equation parameter table of air status

C_0/Pa	C_1	C_2	C_3	C_4	C_5	C_6	E_0 (J/m^3)	V_0
0.1×10^6	0	0	0	0.4	0.4	0	2.5×10^5	1.0

Table 4 Parameters table of φ6 steel bar and steel plate layer materials

Density $\rho/kg.m^{-3}$	Elastic Modulus EX/Pa	Poisson's ratio $NUXY$	Yield Strength $/Pa$	Tangent modulus$/Pa$
7.85×10^3	2.06×10^{11}	0.3	2.35×10^8	2.06×10^9

Table 5 Parameters of aluminum foam materials

Density $\rho/kg.m^{-3}$	Elastic Modulus EX/Pa	Poisson's ratio $NUXY$	Tensile stress at failure $/Pa$
1.2×10^3	1.2×10^9	0.3	1.0×10^7

and can simulate large deformation existing in practical application, and its calculation efficiency and robustness are good. The explosive load is numerically simulated using the high-explosive combustion material model MAT_HIGH_EXPLOSIVE_BURN (MAT_008), combined with the EOS_JWL state function equation. The literature Dobrocinski and Flis (2015), and LS-DYNA Theory Manual (2006) are referenced to define the explosive materials and the equation of state, and the specific parameters are shown in Tables 1 and 2. In the table, ρ is the material density, D is the detonation velocity, PCJ is the pressure of the detonation wave front, k is Bulk modulus, G is Shear modulus, SIGY is yield stress, V0 is the relative volume, E0 is the internal energy per unit volume, and w, A, B, R1, and R2 are the material related constants. Air is simulated using the MAT_NULL material model combined with the linear polynomial equation of the state function (LS-DYNA Theory Manual 2006). Related details are shown in Table 3, C_0-C_6 are the material parameters of air.

Due to the explosion process is very short, the dynamic response time of the structure is very short under the action of explosion load. Therefore, according to the structural dynamic theory, the damping effect is not considered in the numerical calculation of π beam structure under explosion load in this study.

The simulation of concrete and UHPC adopts the MAT_CONCRETE_DAMAGE_REL3 (MAT_72R3) model. The main advantage of this model is based on a single user input parameter, that is, unconfined compressive strength, and the remaining model parameters are automatically generated using built-in algorithms. The model can calculate the elastic modulus of the material by automatically generating the state equation from the input parameters and the stress-strain curve. The damage (Wu and Crawford 2015) and strain rate effects are considered in the model. The compressive strength of concrete is input as 38 MPa, and the parameters of UHPC are taken according to literature (Xu and Wille 2014).

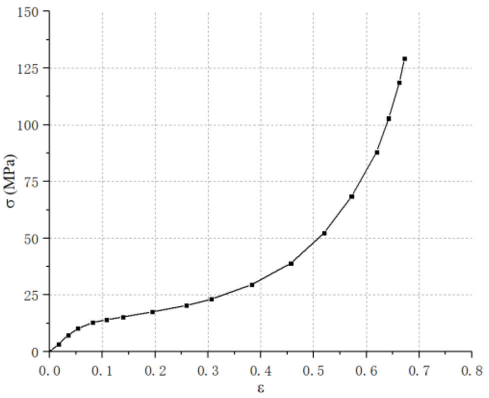

Fig. 3 Stress-strain curve of aluminum foam

The MAT_PLASTIC_KINEMATIC (MAT_003) material model in the LS-DYNA material library is selected to simulate the dynamic characteristics of the steel bar and steel plate protection layer under high strain rates. The specific simulation parameters are shown in Table 4, and the international unit system is adopted. This model is related to the strain rate of the material, which is very suitable for simulating isotropic and dynamic plastic hardening materials. MAT_CRUSHABLE_FOAM (MAT_063) material model is chosen in the material library to model the foam aluminum material. It describes the behavior of the foam by inputting stress and volume strain curves. The stress-strain curve of aluminum foam obtained by SHPB experiment in literature (Wang *et al.* 2003) was adopted, including three stages, as shown in Fig. 3. The specific simulation parameters of the foam aluminum material are shown in Table 5.

3.2 Strain rate effects

Because the strength of the material under the action of high strain rate is stronger than that under the quasi-static action, the study uses the CEB (CEB Bulletin No. 213/214, 1990), and Malvar and Crawford (1998) models to calculate the dynamic amplification factors of the compressive strength and tensile strength of concrete, respectively. Since previous studies have shown that the strain rate effect of ultra-high performance concrete is not obvious, the effect of its strain rate is not considered in this article. The dynamic amplification factor of concrete compressive strength is determined by Eq. (1).

$$DIF_{fc} = \begin{cases} \left(\dfrac{\dot{\varepsilon}}{30\times10^{-6}}\right)^{1.026\times\alpha} & ,\dot{\varepsilon} \le 30s^{-1} \\ \gamma\times\dot{\varepsilon}^{1/3}, 30 < \dot{\varepsilon} \le 300s^{-1} \end{cases} \tag{1}$$

In $\alpha = (5+3f_{cu}/4)^{-1}$, where f_{cu} is the compressive strength of the cube; $\log\gamma = 6.156\alpha - 0.49$.

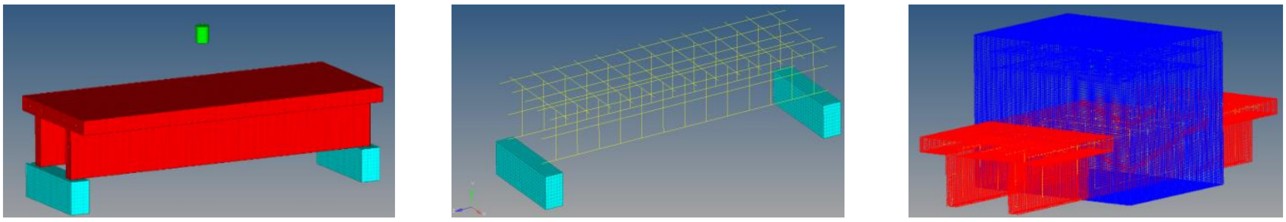

(a) Finite element model of π beam explosion (b) Finite element model of reinforcement in π beam (c) Air domain model of π beam

Fig. 4 Explosion finite element model of π-section beam

(a) Explosion-facing surface of top plate (b) Back- explosion surface of top plate

Fig. 5 Damage effect of π beam in explosion test under Y1 condition

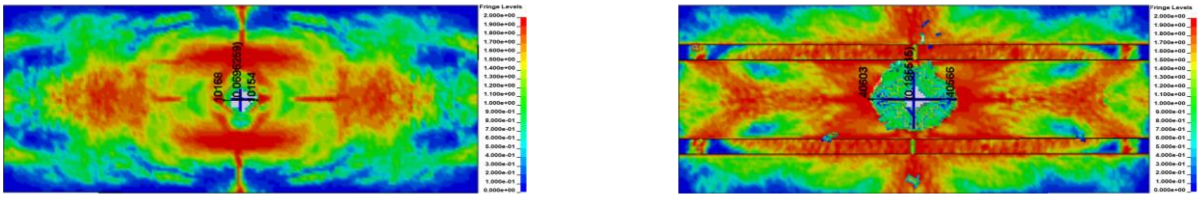

(a) Explosion-facing surface of top plate (b) Back- explosion surface of top plate

Fig. 6 Numerical simulation damage effect of π beam under Y1 condition

The dynamic amplification factor of concrete tensile strength is determined by Eq. (2)

$$DIF_{ft} = \begin{cases} \left(\dfrac{\dot{\varepsilon}}{10^{-6}}\right)^{\delta}, & \dot{\varepsilon} \le 1s^{-1} \\ \beta \times \left(\dfrac{\dot{\varepsilon}}{10^{-6}}\right)^{1/3}, & 1 < \dot{\varepsilon} \le 300s^{-1} \end{cases} \tag{2}$$

In $\delta = 1/(1 + 8f_c'/f_{c0}')$, $f_{c0}' = 10\ MPa$, where f_c' is the uniaxial compressive strength of concrete; $\log\beta = 6\delta - 2$.

3.3 Verification of the finite element model

In order to verify the accuracy and reliability of this numerical model, the numerical model was verified by combining the explosion test results of B series B1 beams (corresponding to the Y1 in this article) in reference (Li *et al.* 2018b). The related results are compared with the test results, and the finite element model is shown in Fig. 4. In this study, the explosive is located in the middle of the span of π beam and above the top surface of the beam for explosion analysis. In the test, the π beam was supported above the concrete cushion stone at the bottom of the beam, and the bottom of the concrete cushion stone was fixed. In the numerical analysis of π beam explosion, the contact between π beam and concrete cushion stone was simulated by using AUTOMATIC_SURFACE_TO_SURFACE contact algorithm in LS-DYNA software. The static friction coefficient was 0.4, the dynamic friction coefficient was 0.3, and the fixed constraint was adopted at the bottom of concrete cushion stone.

In this study, in order to fully reflect the entire explosion process of the π beam, the explosion analysis time of the test beam is 60 ms. Because the mesh size has a great influence on the explosion analysis results, the mesh convergence analysis is carried out and the test results are verified. At the same time, the calculation efficiency andother factors are considered to determine the optimal mesh calculation size. Five mesh sizes of 20 mm, 15 mm, 10 mm, 5 mm and 2 mm were used to calculate the finite element model. Through numerical calculation and analysis, it can be found that with a 5 mm grid, the requirements of numerical calculation stability, accuracy of finite element results and calculation efficiency are balanced, and the calculation results are in ideal agreement with the experimental data. The explosion damage of the π-shaped beam is shown in the Figs. 5 and 6.

$$MA = \frac{(D + D_1) \times S_1}{2} + \frac{(D + D_2) \times S_2}{2} \tag{3}$$

According to reference (Li *et al.* 2018b), in order to accurately describe the blast-damaged area of the π-shaped beam under explosive load, five parameters D1, D2, D, S1 and S2 are used to represent the damaged area, as shown in Fig. 7. H is the thickness of π beam roof. D1 is the diameter of the spalling pit on the top surface of the shock wave incident, D2 is the diameter of the spalling pit on the bottom

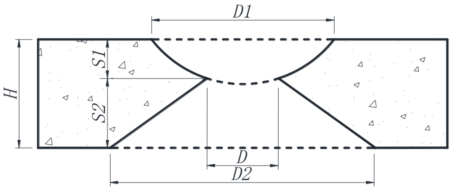

Fig. 7 Parameter diagram of the explosion damage area of π beam

Table 6 π-beam failure area parameter table under Y1 and Y2 working conditions

Damage area parameters	Numerical analysis results S_f	Test results S_e	S_e / S_f
D_1/cm	/	/	/
D_2/cm	18.55	18.10	0.98
D/cm	6.96	6.85	0.98
S_1/cm	/	/	/
S_2/cm	4.40	4.40	1.00
Maximum spalling area of concrete (MA/cm^2)	56.12	54.89	0.98

surface, D is the diameter of the blast hole, S1 is the distance from the edge of the blast hole to the top surface, and S2 is the distance from the edge of the blast hole to the bottom surface. Simultaneously, the maximum spalling area (MA) of concrete is adopted to quantitatively analyze the damaged area of the π-shaped beam in the explosion load. In this paper, the maximum spalling area (MA) of concrete is calculated by the area of the damaged area on the longitudinal section of the π-shaped beam, which can be expressed as the sum of the spalling pit area on the top surface and the spalling pit area on the bottom surface, which can be approximated by Eq. (3). According to Fig. 6, the damage area of π beam was measured by LS-PREPOST software and calculated by formula 3 to obtain the damage area of π beam under blast load. The finite element simulation analysis results and field test failure area parameters for π beam under the action of Y1 and Y2 explosion conditions are shown in Table 6.

Through the calculation and analysis above, it can be seen that the numerical analysis results of the π-shaped beam under the explosion conditions Y1 is in good agreement with the experimental phenomenon, and the failure mode is the same. Under the explosion condition Y1, the numerical analysis results and the experimental damage patterns are given as follows: the top plate of the π beam has explosive penetration failure, the beam web is not damaged, and there is no network cracking. By further comparing the π beam in the finite element analysis of the explosion damage area data and the damage data obtained from the field explosion test, it is found that the damage parameters of the explosion damage area and the maximum concrete spalling area obtained from the test are between 0.98-1.00 of the finite element analysis result, whose error is within 5%. Therefore, it is concluded that the π beam explosion numerical model can more accurately simulate and analyze the dynamic response and damage of reinforced concrete π beams under the explosion, through which following analysis and research can be continued.

4. π-beam explosion protection research

4.1 Time-history curve analysis of the pressure of π beam

4.1.1 Peak values of pressure in different parts of π-beam

Since the damage of the structure under the action of the explosion load mainly depends on the magnitude of the explosion shock wave overpressure and the duration of its action, we analyze the pressure-time history curve of the π beam mid-span section (position directly below the explosion center) under various explosion conditions. The analyzed areas include the front and back explosion surfaces of the top plate, the inside and outside of the web (the section directly below the explosive core is selected). In addition, the pressure-time history curve of each part is the average value of all elements in the section.

Fig. 8 shows the explosion load of the unprotected π beam under the explosive load at a proportional distance of 0.16 m/kg$^{1/3}$ (100g TNT and 7.5 cm). It can be seen from the figure that the pressure is non-uniformly distributed on the surface of the unprotected π beam. Under the action of the explosion load at the proportional distances of 0.16 m/kg$^{1/3}$, the front surface of the unprotected π beam top plate is under the explosion center, and the pressure peak is 36.2 MPa. The pressure peak on the back surface of the top plate is 10.81 MPa. As the shock wave propagates to the web of the π beam, the energy of the shock wave gradually weakens and the pressure peak is relatively reduced. The pressure peak on the inner side of the web is 15 MPa, and the pressure peak on the outer side of the web is -5 MPa.

Table 7 shows the specific values of the pressure peak on front surface and the back surface of the π top plate, the inside and outside of the web for the π beam with different protection conditions.

It can be seen from Table 7 that the time for the shock wave to reach the surface of the protective layer is very short. Similarly, the period during which the positive shock wave acts on the structure is also limited. After the structure undergoes a huge and short-term positive shock wave, the shock wave decays rapidly, and then continues to weaken in the form of an oscillating shock wave, and finally approaches atmospheric pressure. It can be seen from Table 7 that after the π beam is protected by different protection systems, the pressure peak of the each part of the π beam is reduced relative to the unprotected original beam, and the peak value of the pressure drops in different protection conditions. Compared with the unprotected beam, the pressure peak of the front surface of the top plate is reduced by 25%-45%, and the pressure peak on the back surface of the roof is reduced by 21%-31% compared with the unprotected beam. Compared with the unprotected beam, the pressure peak of inside/outside of the web decreased by 6%-31% and 2%-20% respectively.

The analysis shows that the pressure on the back blast facing surface decreases less than the front blast surface. The shock wave is then transmitted to the inside of the web,

(a) Pressure on the top plate under Y1 (b) Inner and outside pressure of the web under Y1

Fig. 8 The pressure time history curve of π beam under unprotected conditions

Table 7 Working conditions for explosion and protection of π beam specimen

Peak value of pressure in each part of π beam (Mpa)	100 g TNT, Detonation center distance: 7.5 cm					The pressure peak ratio (protected /unprotected working condition)			
	Y1	C1	G1	U1	Z1	C1/Y1	G1/Y1	U1/Y1	Z1/Y1
Explosion-facing surface of top plate	36.2	27.3	25.5	22.8	19.8	0.75	0.70	0.63	0.55
Back- explosion surface of top plate	10.8	8.5	7.8	7.6	7.48	0.79	0.72	0.70	0.69
Inside of the web	15.0	14.1	12.8	10.3	11.7	0.94	0.85	0.69	0.78
Outside of the web	-5.0	-4.9	-4.8	-4.0	-4.6	0.98	0.96	0.80	0.92

and the pressure drops to a certain extent. Because the shock wave overpressure is less affected by the protective layer on the outside of the web, and the shock wave on the outside of the web is affected by the reflection of the flange, the pressure peak is basically not reduced on the outside of the π beam web. At the same time, it can be seen from the analysis that after the π beam is protected by the Z1 combined protective layer, the pressure peak of each part of the π beam is significantly reduced. Compared with the unprotected peaks on the front and back explosion surfaces, the inner and outer sides of the web, the top plate of the π beam reduces by 45%, 31%, 22%, and 8%, respectively. And through the analysis of the pressure peak between each protective layer in the combined protection, it is found that the pressure peak passing through the protective layer to the top surface of the π beam is: 43.2 MPa, 38.4 MPa, 23.6 MPa, 19.8 MPa. We can thus conclude that after the peak pressure passes through the foamed aluminum protective layer, the pressure is significantly reduced, and thus this layer serves as a main energy-consuming one.

4.1.2 Longitudinal distribution of the pressure in π-beams under different protective conditions

When the explosion occurs, the pressure is unevenly distributed on the π beam. The peak value of pressure on the front face of the π beam under the explosion center is the largest, and the peak arrival time is the earliest. Then the shock wave propagates to the π beam in both longitudinal and horizontal directions. As the distance gets farther, the pressure on the front, back, and inner and outer sides of the web (the front, back, and side) of the π beam top plate gradually decreases. Affected by different protection systems, the distribution of the explosion load in all directions of the π beam is irregular. Because the longitudinal distance of the beam is relatively large, the longitudinal pressure distribution law can show the peak value of the shock wave after passing through the protective layer. The pattern of change can directly reflect the protective effect of the protective layer. Since the analysis in section 4.1.1 has shown that the protection system has little effect on the pressure on the outside of the web, in this section we only analyze the longitudinal distribution of the pressure along the π beam on the implosion face, the back-burst face and the inside of the web. Through calculation and analysis, the peak value of element pressure at different positions and longitudinal distances of π beam under different protection conditions are shown in Table 8.

Table 8 shows that when the distance from the center of the π beam is 0.125 m, the pressure peak on the top plate of the π beam is between 7.01 MPa and 8.81 MPa under the protection of the four protection conditions C1, G1, U1 and Z1. Compared to the unprotected Y1 working condition, it is attenuated by 35%-48%; the pressure peak of the roof back burst surface is between 5.45 MPa and 6.91 MPa and the attenuation range is 10%-29%; the pressure peak on the side of the web is between 5.65 MPa-6.75 MPa and the attenuation range is 25%-37%. At the distance of 0.25 m from the center, the π beam is protected under working conditions C1, G1, U1, and Z1. The pressure peak on the front surface of the roof is between 4.51 MPa and 7.02 MPa, and the attenuation range is 32% to 56%; The pressure peak of the explosion surface is between 3.58 MPa and 4.17 MPa, and the attenuation range is 12% to 24%; the pressure peak on the inner side of the web is between 4.05 MPa and 4.46 MPa, and the attenuation range is between 11% and 19%. At the distance of 0.375 m from the center, the π beam is protected by working conditions C1, G1, U1 and Z1. The pressure peak on the back of the roof is between 3.51 MPa

Table 8 Pressure peak at different parts and distances of π beam

Peak value of pressure in each part of π beam (Mpa)		100 g TNT, Detonation center distance: 7.5 cm					The pressure ratio under various protection conditions			
		Y1	C1	G1	U1	Z1	C1/Y1	G1/Y1	U1/Y1	Z1/Y1
Explosion-facing surface of top plate	0.000 m	36.20	27.31	25.51	22.80	19.81	0.75	0.70	0.63	0.55
	0.125 m	13.52	7.01	7.72	8.81	7.01	0.52	0.57	0.65	0.52
	0.250 m	10.31	6.62	6.03	7.02	4.51	0.64	0.58	0.68	0.44
	0.375 m	8.13	4.71	4.22	5.51	3.51	0.58	0.52	0.68	0.43
Back-explosion surface of top plate	0.000 m	10.81	8.5	7.78	7.57	7.48	0.79	0.72	0.70	0.69
	0.125 m	7.71	6.91	6.81	6.21	5.45	0.90	0.88	0.81	0.71
	0.250 m	4.72	4.06	4.15	4.17	3.58	0.86	0.88	0.88	0.76
	0.375 m	4.05	3.42	3.23	3.43	3.08	0.84	0.80	0.85	0.76
The inside of the web	0.000 m	15.01	14.11	12.81	10.30	11.71	0.94	0.85	0.69	0.78
	0.125 m	9.02	6.75	6.61	6.12	5.65	0.75	0.73	0.68	0.63
	0.250 m	5.03	4.46	4.26	4.21	4.05	0.89	0.85	0.84	0.81
	0.375 m	4.02	3.58	3.41	3.52	3.03	0.89	0.85	0.88	0.75

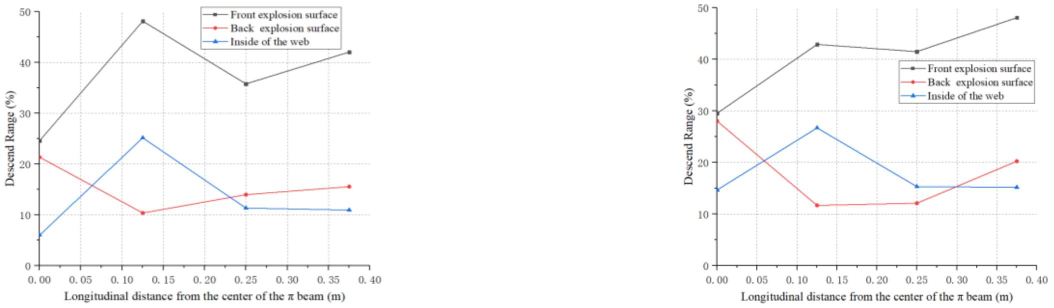

(a) Attenuation curve under condition C1 (b) Attenuation curve under condition G1

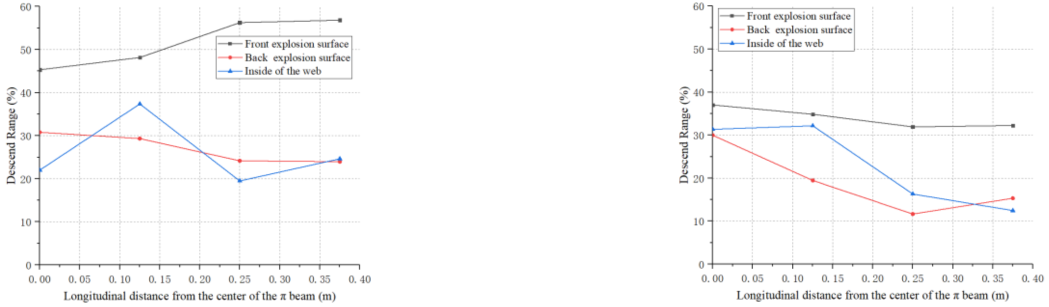

(c) Attenuation curve under condition Z1 (d) Attenuation curve under condition U1

Fig. 9 The attenuation curve of the pressure peak of the π beam along the longitudinal direction under various protection conditions

and 5.51 MPa and the attenuation range is 32% to 57%; The pressure peak of the explosion surface is between 3.08 MPa and 3.43 MPa, and the attenuation range is 15%-24%; the pressure peak on the inner side of the web is between 3.03 MPa-3.58 MPa and the attenuation range is 11%-25%. Under various protection conditions of the π beam, the pressure of π beam at different distances compared with the peak pressure at the same position in the unprotected Y1 working condition is shown in Fig. 9.

As shown in Fig. 9, under the effects of various protection systems, compared with the unprotected π beam, the attenuation amplitude of pressure at different parts is not consistent. Specifically, the pressure peak attenuation amplitude is the largest on the front surface of the top plate. However, the attenuation amplitude is relatively small on the inner side of the web and the back surface of the roof. The main reasons for the difference are that the shock wave pressure loses most of the energy after passing through the top plate protection layer, and the shock wave pressure is relatively small on the back-explosion surface, which makes the attenuation amplitude not obvious. Meanwhile, under the action of various protection conditions, the pressure of the π beam is compared with the unprotected Y1 beam. The pressure peak increases with the longitudinal distance, and the attenuation speed tends to slow down. In addition, under the action of the four protection systems, and the cases where the pressure is at different positions in the longitudinal direction of the π beam, we analyze the attenuation amplitude of the pressure peak at the relative center as Fig. 10.

(a) Attenuation curve under condition Y1 (b) Attenuation curve under condition C1

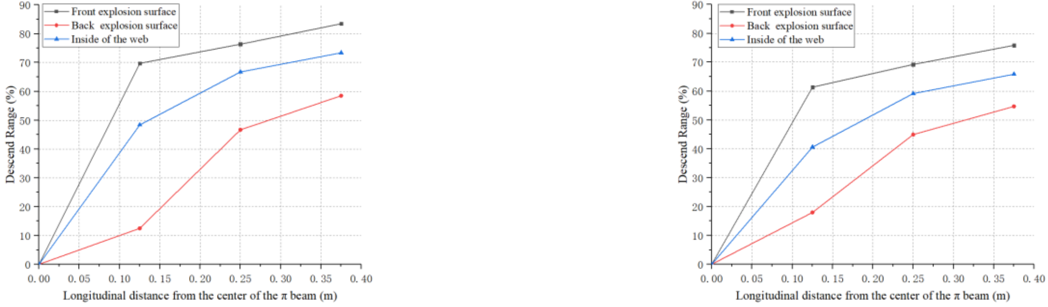

(c) Attenuation curve under condition G1 (d) Attenuation curve under condition U1

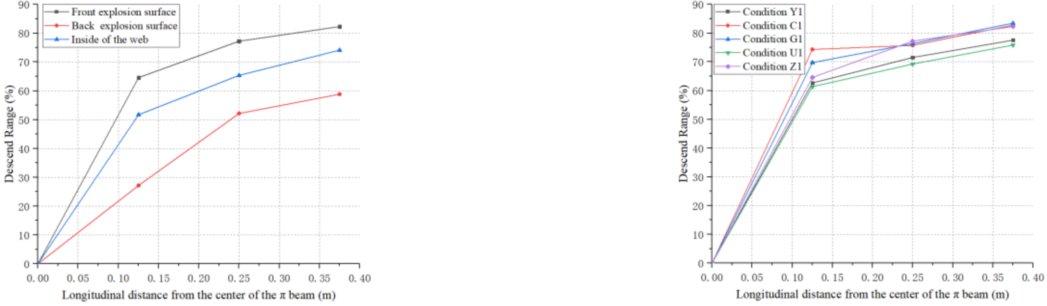

(e) Attenuation curve under condition Z1 (f) Attenuation curve of explosion-facing surface

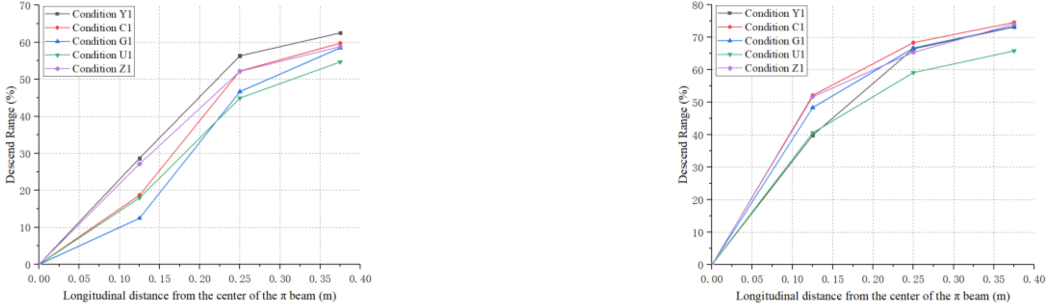

(g) Attenuation curve of back- explosion surface (h) Attenuation curve of the inside of the web

Fig. 10 Attenuation curve of pressure peak at the relative center of the π beam at different longitudinal positions

As Fig. 10 shows, under various explosion conditions, as the longitudinal distance increases, the attenuation amplitudes of the pressure peaks at different parts of the π beam are different with the pressure peaks at its center position. Specifically, the peak attenuation of pressure on the front surface of the roof is larger; the peak attenuation of pressure on the inner side of the web is relatively small; and the peak attenuation of pressure on the back of the roof is the smallest. Second, under different protection conditions, the peak decay speed of pressure of the π beam varies with the increase of the longitudinal distance. Through the analysis of the pressure peak attenuation curve of the impact wave on the front surface, the back surface and the inner side of the web, we have found that the peak of the pressure of the π beam under the combined protection of working condition Z1 attenuates the fastest along the longitudinal direction. At 3/4 of the π beam, the pressure peak attenuation on the front surface is close to 80% while for the inner side of the web is close to 70%, and the attenuation amplitude of the back surface of the roof is 60%.

4.2 Energy analysis of π-beam under different protective conditions

The energy generated by π beam under explosive load consists of kinetic energy, internal energy, contact slip

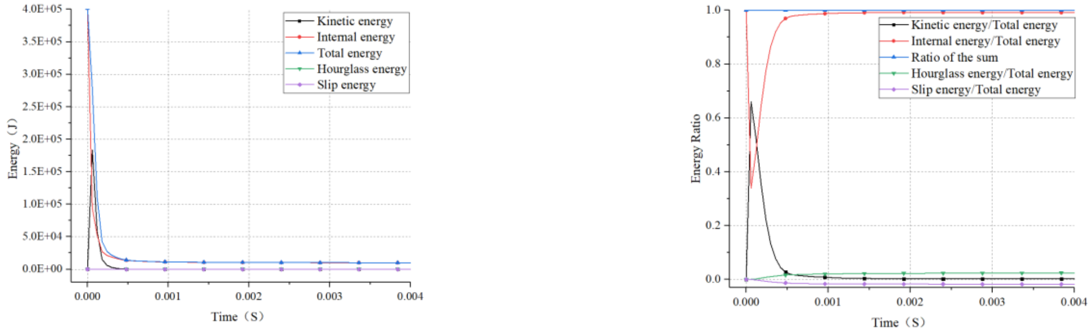

(a) Time history curve of each energy under Z1

(b) Time history curve of the proportion under Z1

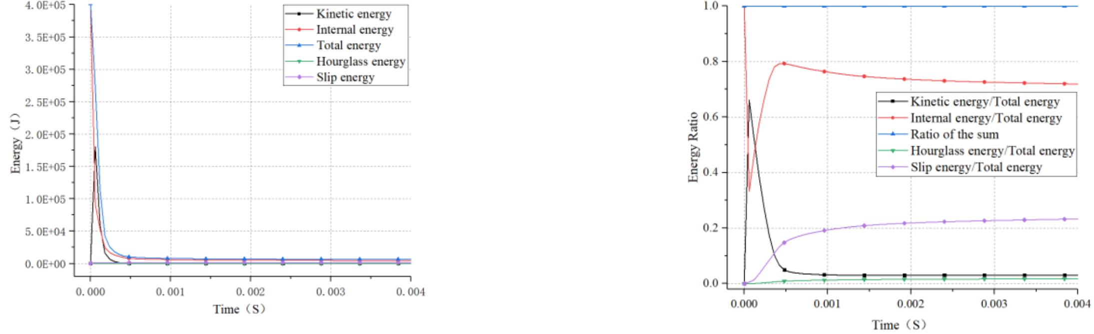

(c) Time history curve of each energy under C1

(d) Time history curve of the proportion under C1

(e) Time history curve of each energy under G1

(f) Time history curve of the proportion under G1

(g) Time history curve of each energy under U1

(h) Time history curve of the proportion under U1

Fig. 11 The time-history curve of each energy and time history curve of the proportion of each energy to the total energy of π beam under various protection conditions

energy and hourglass energy. The paper analyzes the energy changes of the entire π beam and its components under explosive loads when using different protective materials, and then studies the structure’s ability to consume energy generated by the explosion shock wave, and finally analyzes the π beam under various protection conditions from an energy perspective. After the computation analysis, we can obtain the energy distribution patterns of the protection layers and the components of π beam such as concrete and steel bar under explosion loads, and thus study the capability of the protection materials of π beam to consume energy under different conditions.

Fig. 11 shows the time history curve and proportion time history curve of total energy, kinetic energy, internal energy, contact slip energy and hourglass energy of the π beam under various protection conditions under the explosive load of 100 g and the proportional distance of 0.16 m/kg$^{1/3}$.

As shown in Fig. 11, under various protection conditions, the kinetic energy and internal energy of the π beam rise very quickly under the action of the explosion load. The

(a) Energy proportion time history curve under C1 (b) Energy proportion time history curve under G1

(c) Energy proportion time history curve under U1 (d) Energy proportion time history curve under Z1

Fig. 12 Energy time history curve and energy proportion time history curve of each part of π beam

time when the kinetic energy reaches the peak value lags the time when the internal energy reaches the peak value. Although the hourglass energy has increased, the increase is relatively slow, less than 5% of the total energy. At the same time, each energy decays with time, among which the kinetic energy decays more rapidly, and eventually each energy tends to vibrate with a small amplitude. At the beginning of the explosion, internal energy accounts for the largest proportion of total energy, followed by kinetic energy, and hourglass energy and slip energy are the smallest. Subsequently, the proportion of internal energy to the total energy gradually increased, followed by kinetic energy, and the hourglass energy remained the smallest. In each protective working condition, the slip energy in working condition C1 is relatively large. As the explosion shock wave propagates, the total energy of the structure has the largest proportion of the internal energy, followed by the kinetic energy. In the end, both the internal energy and the kinetic energy of the structure tend to stabilize after a small oscillation. The internal energy of the structure is expressed in the form of deformation energy in the macroscopic view. Therefore, improving the overall ductility of the protective main beam helps to improve its anti-explosion ability.

In order to study the energy dissipation mechanism of π beam under explosive load, we analyze the energy of the concrete, steel, and protective layer in the π beam under various protection conditions and the proportion of total energy. Under the action of the explosion load, Fig. 12 shows the energy variation law and proportion time history curve of the concrete part, the reinforced part, and the protective layer of the π beam with different protection forms. The energy of each component of the π beam, such as concrete, steel bars, and protective layer, reaches its peak quickly, and then the small-amplitude oscillation stabilizes.

Meanwhile, as shown in Fig. 12, the energy absorption capacity of each protection layer is different under different protection conditions. The energy consumption of each protective layer in working condition C1 (CFRP protective layer), working condition G1 (steel plate protective layer), working condition U1 (UHPC protective layer) and working condition Z1 (combined protective layer) respectively bear 5%, 18%, 72%, and 90% of the total energy of the three parts of the π beam. Specifically, the π beam concrete part bears 89%, 80%, 26%, 8% of the total energy in the protective beam. The reinforced part bears 6%, 2%, 2%, and 2% of the total energy in the protective beam. Among them, the energy consumption of the top surface layer, the sandwich foam aluminum layer, and the bottom layer of the Z1 combined protective layer account for 3%, 81%, and 6% of the energy of the π beam respectively. Therefore, the Z1 combined protection layer consumes the most energy in the four protection conditions, and the sandwich layer foam aluminum consumes 81% of the energy, which performs relatively well and effectively reduces the damage of the π beam.

According to the above analysis, the energy of π beam under various protection systems under explosion load mainly includes internal energy, kinetic energy, contact slip energy and hourglass energy. The distributions of different forms of energy are basically same between π beam and its components: the internal energy is the largest one, followed by kinetic energy. The hourglass energy is the smallest. All energy time history curves show that the change of energy is closely related to the propagation of stress waves. After the explosion, the kinetic energy and internal energy increase rapidly. As the shock wave continues to propagate, the kinetic energy decays faster. The main part of the internal energy tends to be stable, while the hourglass energy accounts for a relatively small proportion. Second, through the analysis of the energy distribution form of each

(a) Damage to the top surface of the plate under C1 (b) Damage to the back of the plate under C1

(c) Damage to the top surface of the plate under G1 (d) Damage to the back of the plate under G1

(e) Damage to the top surface of the plate under U1 (f) Damage to the back of the plate under U1

(g) Damage to the top surface of the plate under Z1 (h) Damage to the back of the plate under Z1

Fig. 13 π beam explosion damage under different protection conditions

protective beam in working conditions C1, G1, U1 and Z1, it is found that the combined protective layer in working conditions Z1 has better energy consumption capacity and the highest proportion of absorbed energy. The largest energy consumption in the protective layer is the foam aluminum interlayer, which effectively reduces the damage of the π beam under the explosion load.

4.3 Failure mode of the π-beam

When the explosion occurs, the top of π beam is under the major pressure. The internal strain is disturbed and propagate to the double side of web and the back burst surface of the roof of the beam, in the form of compressional waves. The waves then reflect, serving as tensile waves. When the tensile stress generated by the reflected wave is larger than the summation of compressional stress and the tensile strength, the concrete will disrupt and spall. The resulted shearing and bending stress will lead to the disruption of the mortar within the coarse aggregate, followed by a local damage of the beam. In order to implement an accurate analysis of the damaged area of the π beam, we adopt a set of parameters D1, D2, D, S1 and S2 as shown in Fig. 7, in order to provide a complete description of the damaged area of the π beam.

The failure modes of different working conditions is shown in Fig. 13. The test results show that the failure mode with protection is mainly persistent crack and local spalling on the roof, rather than integral deformation. The range of damage is relatively limited compared to that of unprotected beam, and the web and flange do not show obvious damage. The failure mode of roof is the spalling of the front and back blast faces affected by the compressional wave and reflected wave, which generates funnel shaped pits. The front area of pits and the back area of spalling interact with each other, resulting in the failure of the persistent cracks on the roof. The steel bars of the beam is locally deformed under the core of explosion, instead of thorough failure.

As shown in Fig. 5(a), the top plate of the unprotected π beam will undergo penetration damage and the concrete peeling damage on the back-blast surface under the action of the explosion load. When different forms of protection are adopted, due to the various protective effects of each protective layer, the degree of damage of the π beam under the action of the explosion load is also different, shown in Fig. 13. The explosion damage pattern of the π beam under the protection of working condition C1 has not changed; that is, penetration and concrete spalling damage has also occurred, which is consistent with the Y1 beam. Under the

Table 9 π beam damage area parameter table under different protection conditions

Damage area parameters	100 g TNT, Proportional distance z=0.16 m/kg$^{1/3}$					Damaged area parameter ratio			
	Y1	C1	G1	U1	Z1	C1/Y1	G1/Y1	U1/Y1	Z1/Y1
D_1/cm	/	/	20.04	7.92	8.99	/	/	/	/
D_2/cm	18.55	17.19	11.15	16.07	13.55	0.93	0.60	0.87	0.73
D/cm	6.96	7.49	2.31	4.05	1.95	1.08	0.33	0.58	0.28
S_1/cm	/	/	1.46	1.96	1.47	/	/	/	/
S_2/cm	4.40	4.40	2.94	2.44	2.93	1.00	0.67	0.55	0.67

protection of working conditions G1, U1 and Z1, due to the protective layer of the π beam, the concrete peeling damage on the front face of the top slab will be limited, and the spalling area of the concrete on the back burst face will be relatively reduced, which is slightly different from the working condition C1. The specific parameters of the damaged area of the π beam under each working condition are shown in Table 9.

According to Fig. 13 and Table 9, we find that the π beam in working condition C1 is protected by the CFRP layer. When the explosion occurs, the explosion shock wave propagates quickly to the surroundings, and the compressional wave initially acts on the CFRP fiber layer on the front face of the π beam top plate. When the CFRP reaches the ultimate strain and breaks, the compressional wave continues to propagate to both sides of the π beam web and the back-burst surface. After the CFRP fractures, the roof concrete is subjected to greater tensile stress, and thus begins to peel off. The shock wave causes penetrating damage to the top surface of the π beam, and the back blast surface is also damaged. The diameter of the spalling damaged area on the bottom surface of the π beam top plate is 17.19 cm, and the diameter of the penetrating hole is 7.49 cm. Because the CFRP protective layer is thinner, the CFRP fiber layer is broken and torn under the action of explosive load. The CFRP layer is subjected to a larger shock wave during the tearing process, causing the corresponding roof concrete to be locally damaged. Therefore, the diameter of the penetrating hole in the roof of the working condition C1 is larger than that of the unprotected π beam.

In working condition G1 steel plate layer protection calculation, due to the high strength of the steel plate, the steel plate protection layer has no damage, and only local deformation and local plastic strain occur under the core of the explosion. Through the analysis of the damage area of the top slab of the concrete beam under the steel plate layer, it is shown that after the shock wave passes through the steel plate layer, the shock wave reflects at the bottom of the layer to form a tensile wave, causing the roof concrete spalling damage. At the same time, the steel plate is partially affected by the shock wave. It peels from the roof concrete, and the shock wave makes the larger roof surface to peel off locally. The damaged area is elliptical with a maximum diameter of 20.5 cm. The flanges and webs of the π beam are not damaged. In addition, due to the high strength of the steel plate layer, it effectively slows down the damage of the shock wave, resulting in the small π beam roof penetration damage and back explosion surface peeling damage. The diameter of the top plate penetrating hole is 2.31 cm, and the top plate back explosion surface peeling diameter is 11.15 cm. Compared with the unprotected working condition Y1, the steel plate protection caused a certain degree of spalling damage on the front surface of the top plate, but the spalling was thinner. Besides, the steel plate has a buffer effect on the shock wave, and thus under the steel plate protection, the penetration damage of the top plate of the π beam and the surface spalling damage of the back-burst plate is not that severe.

As shown in Figs. 13 (e) and (f), the protective effect of the UHPC layer of the π beam in the working condition U1 is similar to that of the steel plate layer. The strength of the UHPC layer is smaller than that of the steel plate. The shock wave generated by the explosion directly acts on the UHPC protective layer, which will generate penetration damage to the UHPC layer. The shock wave is reflected after passing through the protective layer, causing the top plate of the π beam to peel off and damage locally to form a blast hole. Since UHPC has a smaller strength than steel plates and better energy absorption, the concrete spalling damaged area on the front face of the roof is smaller than the working condition G1 and the unprotected π beam. The diameter is 7.92 cm, and the diameter of the penetrating hole is 4.05 cm. Both the flange and web of the π beam are not damaged. When the shock wave is transmitted to the back-blast surface of the roof, the reflection of the shock wave causes the concrete damage on the back-blast surface to peel off, with a diameter of 16.07 cm. In the calculation of working condition Z1 combined protection layer, the steel plate layer on the top surface of the combined protection layer has local deformation and local damage. However, due to the efficient energy dissipation capacity of the foamed aluminum layer in the middle layer, the shock wave generates less damage to the π beam after passing through the combined protective layer. The diameter of the concrete spalling area on the front surface of the roof is 8.99 cm, the diameter of the penetrating hole is 1.95 cm. The diameter of the damaged area was 13.55 cm, and neither the flange nor the web is damaged. The results show that under the action of working condition C1, G1, U1 and Z1, the diameter of the spalled area of the bottom plate accounts for 93%, 60%, 87% and 73% of the top plate respectively, compared with the unprotected π-shaped beam. The hole diameters account for 108%, 33%, 58%, and 28% for the four working conditions respectively.

Through the above analysis, we have shown that under the action of explosive load, the damaged area of the π

Table 10 Maximum concrete spalling area of π beam under different protection conditions and protection efficiency of each protection layer

Parameter	100 g TNT, Proportional distance Z=0.16 m/kg$^{1/3}$				
	Unprotected π beam under Y1	C1	G1	U1	Z1
MA (cm²)	56.12	54.30	36.11	36.28	30.75
d	/	0.97	0.64	0.65	0.55
ρ (%)	/	3%	36%	35%	45%

beam under the combined protection of working conditions Z1 is smaller and the protective effect of the combined protective layer of other protection working conditions is more stable. Due to the role of the intermediate energy-dissipating layer, the explosion shock wave passes through the protective layer to the π beam more smoothly, which greatly reduces the destructive force of the explosion impact. The limitation of finite element simulation is that it cannot consider the influence of factors such as fire and high temperature. Therefore, the damaged area in actual explosion protection is larger than the damaged area calculated by simulation.

4.4 Protection efficiency of π-beam under different protection conditions

The protective efficiency ρ for the protective layers of the beam was calculated using the largest spalling area for concrete of the beam under explosion loads. Specific calculation methods are shown in Eq. (4).

$$\rho = 1 - d, d = \{(MA_1)/(MA_0)\} \qquad (4)$$

where MA_0 is the largest spalling area of concrete for π beam without protection under explosive load; MA_1 is the largest spalling area of concrete for π beam with protection under explosive load. The calculation for MA is based on Eq. (3). The obtained largest spalling area of concrete for π beam and the protection efficiency is provided in Table 10.

As shown in Table 10, under the condition mentioned above, the largest spalling area of concrete for π beam without protection is 56.12 cm². In comparison, this value becomes 54.30 cm², 36.11 cm², 6.28 cm², 30.75 cm² for working condition C1, G1, U1 and Z1 with protection. The protection efficiency for the combination of different protection layers and working condition falls in the range of 3% to 45%. Specifically, the working condition Z1 has the highest protection efficiency 45%, while the CFRP layer of the working condition C1 only has 3%, the smallest one of all. The efficiency of combinational protection layer of Z1 is about 1.3 times of that for working conditions G1 and U1. The failure mode of Z1 further demonstrates this analysis: under this working condition, the damaged areas are relatively smooth for blast face and back burst surface of the roof; the penetrating damage of the roof caused by the explosion is the smallest; the diameter of the detonation hole is only 1.95 cm, which is 28%, 26%, 84%, 48% for working conditions Y1, C1, G1, U1, respectively. It indicates that the combinational protection layers can effectively improve the capability to resist explosion for steel-reinforced concrete π beam. The aluminum foam layer can effectively consume the energy, which forms a well-performed protection integrity with steel plate deployed on the top and bottom of the combinational protection layers, avoiding the fast loss of efficacy of the aluminum foam layers under the explosion.

5. Conclusions

This paper studies the blast resistance performance of reinforced concrete π beams, and draws the following conclusions:

(1) Through comparative analysis with the π beam explosion test, the correctness of π beam explosion finite element analysis model was verified. Meanwhile, we conduct grid convergence analysis on the numerical calculation model, and determine the 5 mm grid analysis size. This numerical model can effectively analyze the dynamic response of the π beam under the action of the explosion load after the protection.

(2) The pressure peaks of the top blast surface, back blast surface, and inner and outer sides of the web under various protective conditions of the π beam were compared and analyzed. Meanwhile, compared to unprotected π beams, with the increase of the longitudinal distance, the peak attenuation amplitude of the pressure is the largest on the front surface of the roof, and the attenuation speed tends to slow down. In addition, under the combined protection of working condition Z1, the pressure peak of the beam attenuates quickly along the longitudinal direction of the beam, and the peak attenuation of the pressure on the front face of the roof is the largest.

(3) By studying the law of energy dissipation of π beams under different working conditions under explosive loads, we find that the total energy of π beams is conserved under the action of explosions. Hourglass energy accounts for much less than 5% of the total energy, and internal energy accounts for the main part. In addition, we have also studied the law of energy consumption of the protective layer under various working conditions and found that the energy of the protective layer under each working condition accounts for the largest proportion of the internal energy. The combined protective layer in working condition Z1 consumes the most energy. The largest energy consumption in the protective layer is the foamed aluminum interlayer, which consumes 88% of the total energy of the three parts of the π beam (concrete, steel, and protective layer).

(4) The failure mode of the beam after protection by the protective layer is partial failure without overall deformation. Flange plates and webs are not damaged. The failure mode is a funnel-shaped concrete spalling pit on the front and back explosion surfaces. In comparison, we find that the structural damage of the π beam is inconsistent under different protection forms, and the damage area is relatively small under the Z1 combined protection.

(5) By using the maximum spalling area of concrete to study the protection efficiency of π beams under different

protection conditions. It can be calculated that the protection efficiency of working condition C1, G1, U1 and Z1 are 3%, 36%, 35% and 45% respectively. Specifically, the protection efficiency of the CFRP layer is at least 3%, and the protection efficiency of the combined protection layer in working condition Z1 is about 1.3 times that of working conditions G1 and U1, which demonstrates the capability of the proposed protection.

References

Abedini, M. and Zhang, CW. (2021), "Dynamic vulnerability assessment and damage prediction of RC columns subjected to severe impulsive loading", *Struct. Eng. Mech.*, **77**(4), 441-461. https://doi.org/10.12989/sem.2021.77.4.441.

Aoude, H., Dagenais, F.P., Burrell, R.P. and Saatcioglu, M. (2015), "Behavior of ultra-high performance fiber reinforced concrete columns under blast loading", *Int. J. Impact Eng.*, **80**, 185-202. https://doi.org/10.1016/j.ijimpeng.2015.02.006.

ASCE Task Committee. (1997), *Design of Blast Resistant Buildings in Petrochemical Facilities*, ASCE, New York, NY, USA.

Castedo, R., Segarra, P., Alanon, A., Lopez, L.M., Santos, A.P. and Sanchidrian, J.A. (2015), "Air blast resistance of full-scale slabs with different compositions: Numerical modeling and field validation", *Int. J. Impact Eng.*, **86**, 145-156. https://doi.org/10.1016/j.ijimpeng.2015.08.004.

Chen, F., Zhong, Y., Gao, X., Jin, Z. and He, X. (2020), "Non-uniform model of relationship between surface strain and rust expansion force of reinforced concrete", *Sci. Rep.*, **11**, 8741. https://doi.org/10.1038/s41598-021-88146-2.

Chen, F., Jin, Z., Wang, E., Wang, L., Jiang, Y., Guo, P., Gao, X. and He, X. (2021), "Relationship model between surface strain of concrete and expansion force of reinforcement rust", *Sci. Rep.*, **11**, 4208. https://doi.org/10.1038/s41598-021-83376-w.

CEB Bulletin No. 213/214, (1993), *CEB-FIP MODEL CODE 1990*, Thomas Telford Ltd., London, UK.

Dobrocinski, S. and Flis, L. (2015), "Numerical simulations of blast loads from near-field ground explosions in air", *Studia Geotechnica et Mechanica*, **37**(4), 11-18. https://doi.org/10.1515/sgem-2015-0040.

Feng, J., Zhou, Y.Z., Wang, P., Wang, B., Zhou, J.N., Chen, H.L., Fan, H.L. and Jin, F.N. (2017), "Experimental research on blast-resistance of one-way concrete slabs reinforced by BFRP bars under close-in explosion", *Eng. Struct.*, **150**, 550-561. https://doi.org/10.1016/j.engstruct.2017.07.074.

Han, G.Z., Yan, B. and Yang, Z. (2019), "Damage model test of prestressed T beam under explosion load", *IEEE Access*, **7**, 135340-135351. https://doi.org/10.1109/ACCESS.2019.2940037.

Hetherington, J. and Smith, P. (1994), *Blast and Ballistic Loading of Structures*, Crc Press, Boca Raton, Florida, USA.

Kee, J.H., Park, J.Y. and Seong, J.H. (2019), "Effect of one way reinforced concrete slab characteristics on structural response under blast loading", *Adv. Concrete Constr.*, **8**(4), 277-283. http://dx.doi.org/10.12989/acc.2019.8.4.277.

Kinney, G.F. and Graham, K.J. (1985), *Explosive Shocks in Air*, Springer, Berlin, Heidelberg, Germany.

Li, J. and Hao, H. (2011), "A two-step numerical method for efficient analysis of structural response to blast load", *Int. J. Protective Struct.*, **2**(1), 103-126. https://doi.org/10.1260/2041-4196.2.1.103.

Li, Y., Algassem, O. and Aoude, H. (2018a), "Response of high-strength reinforced concrete beams under shock-tube induced blast loading", *Constr. Build. Mater.*, **189**, 420-437. https://doi.org/10.1016/j.conbuildmat.2018.09.005.

Li, Z., Liu, Y., Yan, J.B., Yu, W.L. and Huang, F.L. (2018b), "Experimental investigation of p-section concrete beams under contact explosion and close-in explosion conditions", *Def. Technol.*, **14**(5), 190-199. https://doi.org/10.1016/j.dt.2018.07.025.

Livermore Software Technology Corporation, LS-DYNA Theory Manual. (2006), http://www.lstc.com/pdf/ls-dyna_theory_manual_2006.pdf

Malvar, L.J. and Crawford, J.E. (1998), "Dynamic increase factors for concrete", Report No. 0704-0188; 28th DDESB Seminar, Orlando, FL, USA.

Mou, B. and Bai, Y. (2018), "Experimental investigation on shear behavior of steel beam-to-cfst column connections with irregular panel zone", *Eng. Struct.*, **168**, 487-504. https://doi.org/10.1016/j.engstruct.2018.04.029.

Nagy, N., Mohamed, M. and Boot, J. C. (2021), "Nonlinear numerical modelling for the effects of surface explosions on buried reinforced concrete structures", *Geomech. Eng.*, **2**(1), 1-18. https://doi.org/10.12989/gae.2010.2.1.001.

Qi, C., Remennikov, A., Pei, L.Z., Yang, S., Yu, Z.H. and Ngo, T.D. (2017), "Impact and close-in blast response of auxetic honeycomb-cored sandwich panels: Experimental tests and numerical simulations", *Compos. Struct.*, **180**, 161-178. https://doi.org/10.1016/j.compstruct.2017.08.020.

Qu, Y., Li, X., Kong, X., Zhang, W. and Wang, X. (2016), "Numerical simulation on dynamic behavior of reinforced concrete beam with initial cracks subjected to air blast loading", *Eng. Struct.*, **128**, 96-110. https://doi.org/10.1016/j.engstruct.2016.09.032.

RKM FEMA 426, (2003), Reference Manual to Mitigate Potential Terrorist Attacks against Buildings, Federal Emergency Management Agency, USA.

Shadabfar, M., Huang, H.W., Wang, Y. and Wu, C.L. (2020), "Monte Carlo analysis of the induced cracked zone by single-hole rock explosion", *Geomech. Eng.*, **21**(3), 289-300. http://dx.doi.org/10.12989/gae.2020.21.3.289.

Shi, Y., Hao, H. and Li, Z.X. (2008), "Numerical derivation of pressure–impulse diagrams for prediction of RC column damage to blast loads", *Int. J. Impact Eng.*, **35**(11), 1213-1227. https://doi.org/10.1016/j.ijimpeng.2007.09.001.

TM 5-855-1. (1986), Fundamentals of Protective Design for Conventional Weapons, Technical Manual, US Department of the Army, Washington DC, USA.

Wang, W., Liu, R. and Wu, B. (2014), "Analysis of a bridge collapsed by an accidental blast loads", *Eng. Fail. Anal.*, **36**, 353-361. https://doi.org/10.1016/j.engfailanal.2013.10.022.

Wang, Y.G., Hu, S.S. and Wang, L.L. (2003), "Shock attenuation in aluminum foams under explosion loading", *Explosion Shock Waves*, **23**(6), 516-522. http://www.en.cnki.com.cn/Article_en/CJFDTOTAL-BZCJ200306006.htm

Williams, G.D. and Williamson, E.B. (2012), "Procedure for predicting blast loads acting on bridge columns", *J. Bridge Eng.*, **17**(3), 490-499. https://doi.org/10.1061/(ASCE)BE.1943-5592.0000265.

Wu, C. and Sheikh, H. (2013), "A finite element modelling to investigate the mitigation of blast effects on reinforced concrete panel using foam cladding", *Int. J. Impact Eng.*, **55**, 24-33. https://doi.org/10.1016/j.ijimpeng.2012.11.006.

Wu, Y. and Crawford, J.E. (2015), "Numerical modeling of concrete using a partially associative plasticity model", *J. Eng. Mech.*, **141**(12), 04015051. https://doi.org/10.1061/(ASCE)EM.1943-7889.0000952.

Xu, D., Liu, Q., Qin, Y. and Chen, B. (2020), "Analytical approach for crack identification of glass fiber reinforced polymer–sea sand concrete composite structures based on strain dissipations", *Struct. Health Monit.*, 147592172097429. https://doi.org/10.1177/1475921720974290.

Xu, M. and Wille, K. (2014), "Calibration of K&C Concrete Model for UHPC in LS-DYNA", *Adv. Mater. Res.*, **1081**, 254-259. https://doi.org/10.4028/www.scientific.net/AMR.1081.254.

Yan, B., Liu, F., Song, D. and Jiang, Z.G. (2015), "Numerical study on damage mechanism of RC beams under close-in blast loading", *Eng. Fail. Anal.*, **51**, 9-19. https://doi.org/10.1016/j.engfailanal.2015.02.007.

Yao, S.J., Zhang, D., Lu, F.Y., Wang, W. and Chen, X.G. (2016), "Damage features and dynamic response of RC beams under blast", *Eng. Fail. Anal.*, **62**, 103-111. https://doi.org/10.1016/j.engfailanal.2015.12.001.

Zhang, C., Gholipour, G. and Mousavi, A.A. (2019), "Nonlinear dynamic behavior of simply supported RC beams subjected to combined impact-blast loading", *Eng. Struct.*, **181**, 124-142. https://doi.org/10.1016/j.engstruct.2018.12.014.

Zhang, D., Yao, S.J., Lu, F., Chen, X.G., Lin, G.H., Wang, W. and Lin, Y.L. (2013), "Experimental study on scaling of RC beams under close-in blast loading", *Eng. Fail. Anal*., **33**, 497-504. https://doi.org/10.1016/j.engfailanal.2013.06.020.

Zhang, W., ASCE, M., Tang, Z., Yang, Y. and Wei, J. (2021), "Assessment of FRP–concrete interfacial debonding with coupled mixed-mode cohesive zone model", *J. Compos. Constr.*, **25**(2). https://doi.org/10.1061/(ASCE)CC.1943-5614.0001114.

CC